PERGAMON

International Journal of Heat and Mass Transfer 43 (2000) 4101–4118

International Journal of HEAT and MASS TRANSFER

www.elsevier.com/locate/ijhmt

Development of the miniaturized four-sensor conductivity probe and the signal processing scheme

S. Kim*, X.Y. Fu, X. Wang, M. Ishii

Thermal-Hydraulics Reactor Safety Laboratory, School of Nuclear Engineering, Purdue University, 1290 Nuclear Engineering Building, West Lafayette, IN 47907-1290, USA

Received 29 October 1999; received in revised form 26 January 2000

Abstract

The objective of the present study is to develop a miniaturized four-sensor conductivity probe, applicable to a wide range of two-phase flows to obtain the time-averaged local two-phase flow parameters of various types of bubbles. Experimental data acquired by the probe are categorized into two groups in view of two-group interfacial area transport: namely spherical/distorted bubbles as Group 1 and cap/Taylor bubbles as Group 2. Benchmark experiment employing the image analysis method is performed. The results from the benchmark experiment assess both the measurement principle and signal processing scheme of the newly developed four-sensor conductivity probe method.

1. Introduction

In two-phase flows, the interfacial area concentration and void fraction are the key geometric parameters in view of interfacial transport and heat transfer. In order to assess the given two-phase flow systems accurately, the formulation using the two-fluid model [1] can be employed, which is based on the detailed treatment of the phase interactions at the interface. In view of practical applications, Ishii and Mishima [2,3] simplified the two-fluid model as

$$\frac{\partial \alpha_k \rho_k}{\partial t} + \nabla(\alpha_k \rho_k v_k) = \Gamma_k; \quad \text{Continuity} \tag{1}$$

$$\frac{\partial \alpha_k \rho_k v_k}{\partial t} + \nabla(\alpha_k \rho_{kv_k} v_k) = -\alpha_k \nabla p_k + \nabla \alpha_k \left(\bar{\tau} + \tau_k'\right) + \alpha_k \rho_k g + v_{ki}\Gamma_k + M_{ik} - \nabla \alpha_k \tau_i; \tag{2}$$

Momentum

$$\frac{\partial \alpha_k \rho_k H_k}{\partial t} + \nabla(\alpha_k \rho_k H_k v_k) = -\nabla \alpha_k \left(\bar{\bar{q}}_k + q_k^t\right) + \alpha_k \frac{D_k}{Dt} p_k + H_{ki}\Gamma_k + \frac{q_{kt}''}{L_s} + \phi_k; \tag{3}$$

Enthalpy energy

where Γ_k, M_{ik}, τ_i, q_{ki}'' and ϕ_k are the mass generation, generalized interfacial drag, interfacial shear stress, interfacial heat flux and dissipation, respectively, with

* Corresponding author. Tel.: +1-765-494-5759; fax: +1-765-494-5951.

E-mail address: seungjin@ecn.purdue.edu (S. Kim).

0017-9310/00/$ - see front matter
PII: S0017-9310(00)00046-6

Nomenclature

A	area
A_s	measurement area formed by the probe sensors
a_i	interfacial area concentration
D	diameter
D_{ds}	maximum spherical bubble limit
D_{dmax}	maximum distorted bubble limit
D_{cmax}	maximum cap bubble limit
$\boldsymbol{F}$	force
g	gravitational constant
H	enthalpy
h	heat transfer coefficient
j	total superficial velocity
L	length
L_s	length scale
l_s	separation distance between the probe sensors
M_{ik}	generalized interfacial drag
N	number
N_{μ_f}	liquid viscosity number
$\boldsymbol{n}$	unit normal vector
Q	volumetric flow rate
q''	heat flux
Re	Reynolds number
T	total time
t	time
V	voltage
$\boldsymbol{v}$	velocity
v_{iz}	the z-component of the jth interfacial velocity
v_r	relative velocity
v_b'	fluctuation of bubble velocity

Greek symbols

α	void fraction
α_0	maximum angle possible in μ_j
Γ	rate of mass generation
ϕ_j	angle between the bubble interfacial velocity and the unit normal vector of the jth interface
ϕ	energy dissipation rate of the kth phase
μ_j	angle between the probe sensor and the unit normal vector of the jth bubble interface
ν	kinematic viscosity
ρ	density
σ	surface tension
σ_z	velocity fluctuation
τ	shear stress

Subscripts

b	bubble
D	standard drag
eff	effective
f	liquid or front bubble interface
g	gas
h	hydraulic
i	interfacial
k	kth-phase
m	mixture
min	minimum
miss	missing bubble interface
max	maximum
norm	normalized
r	rear bubble interface
s	slug bubble
sm	Sauter mean
tot	total
v	virtual mass
t	time-averaged

the subscript i denoting the value at the interface. Here, L_s denotes the length scale at the interface, where $1/L_s$ has the physical meaning of the interfacial area per unit mixture volume [1], such that

$$\frac{1}{L_s} = a_i; \quad \text{Interfacial area per unit mixture volume} \tag{4}$$

In Eqs. (1)–(3), the interfacial transfer terms can be modeled such that [4–8]

$$\Gamma_k \equiv a_i m_k; \quad \text{Generation of mass} \tag{5}$$

$$M_{id} = \frac{\alpha_d \boldsymbol{F}_D}{B_d} + \frac{\alpha_d \boldsymbol{F}_v}{B_d} + \frac{9}{2}\frac{\alpha_d}{r_d}\sqrt{\frac{\rho_c \mu_m}{\pi}} \int_t \frac{D_d}{D\xi}(\boldsymbol{v}_d - \boldsymbol{v}_c)\frac{d\xi}{\sqrt{t-\xi}}; \tag{6}$$

Generalized drag

$$\Gamma_k H_{ki} + \frac{q''_{ki}}{L_s} = a_i\left[m_k H_{ki} + h_{ki}(T_i - T_k)\right]; \tag{7}$$

Interfacial energy transfer

Here, m_k, F_D, B_d, F_v, and μ_m are the mean mass transfer rate, standard drag force, volume of a typical dispersed fluid particle, virtual mass force and mixture

viscosity, respectively. With the last term in the right hand side of Eq. (6) being the Basset force, the interfacial transfer term due to standard drag can be written in terms of interfacial area concentration [7,8] such that

$$\frac{\alpha_d \boldsymbol{F}_D}{B_d} = -a_i\left[\frac{C_D}{4}\left(\frac{r_{sm}}{r_D}\right)\frac{\rho_c \boldsymbol{v}_r|\boldsymbol{v}_r|}{2}\right] \tag{8}$$

For the interfacial energy transfer term, the interfacial heat flux, q''_{ki} can be modeled using the driving force or the potential for an energy transfer. Hence, in Eq. (7), T_i and T_k are the temperature at the interface and the bulk temperature based on the mean enthalpy, and h_{ki} is the interfacial heat transfer coefficient. The importance of the interfacial area concentration is now evident. As shown in Eqs. (5)–(8), the phase interaction terms are expressed in terms of interfacial area concentration and the driving force such that

$$(\text{Interfacial transfer term}) \sim a_i \times (\text{Driving force}) \tag{9}$$

Therefore, the closure relation and the detailed measurement method for the interfacial area concentration are indispensable for accurate assessment of the given two-phase flows using the two-fluid model.

In efforts of solving the closure problem in the two-fluid model, Kocamustafaogullari and Ishii [9] generalized the population balance approach suggested by Reyes [10] and established the foundation in developing the interfacial area transport equation. Recently, the one-group interfacial area transport equation for dispersed bubbles was formulated by Wu et al. [11]. Nevertheless, it cannot describe the transport phenomena correctly for the bubbles whose shapes vary significantly from spherical, such as cap or slug flows. This is due to the fact that the interaction mechanisms and transport phenomena bubbles are significantly different depending on their size, shape, interfacial area, interfacial drag, or motion. Therefore, two interfacial transport equations should be introduced accounting for the different mechanisms in bubble interactions; namely, Group 1 for spherical/distorted bubbles, and Group 2 for cap/slug/churn-turbulent bubbles. However, the database available for evaluating the theoretical model is far short from being sufficient. Therefore, the development of a reliable local measurement method, which is applicable to a wide range of two-phase flows is indispensable in the development of the two-group interfacial area transport equation.

The conductivity probe has been one of the most widely used measurement techniques in obtaining local two-phase flow parameters [12–20]. It was first proposed by Neal and Bankoff [12] accounting for the fundamental differences in conductivity between water and air. In an air–water two-phase mixture, the characteristic rise/fall of impedance signals from the sensor(s) can be acquired as bubbles pass through the sensor(s) as illustrated in Fig. 1. With the acquired signals from the sensor, the local time-averaged void fraction can be easily obtained by dividing the sum of the time fraction occupied by gas-phase by the total measurement time. Furthermore, its capability of measuring the local interfacial velocity of bubbles with multiple sensors makes the conductivity probe the most popular measurement technique in recent experimental studies. Currently, there exist two types of conductivity probes depending on the flow regimes of application, namely the double-sensor conductivity probe and the four-sensor conductivity probe. The double sensor conductivity probe has been employed in dispersed bubbly flow conditions in many previous studies [13–15,17,19,20], whereas the four-sensor probe has been applied in cap or slug flow conditions [16,22].

2. Measurement principle

The measurement principle of the multi-sensor conductivity probe in obtaining local time-averaged interfacial area concentration, a_t, is based on the definition given by Ishii [1], where the local time-averaged $\bar{a}^t_i$ is defined by

$$\bar{a}^t_i = \frac{1}{\Delta T}\sum_j\left(\frac{1}{|\boldsymbol{v}_i \cdot \boldsymbol{n}_i|}\right)_j \tag{10}$$

where j denotes the jth interface which passes a local point during the time interval, ΔT. Here, $\boldsymbol{v}_i$ and $\boldsymbol{n}_i$ are the bubble interfacial velocity and unit surface normal vector of the jth interface, respectively. Eq. (10) implies that the local interfacial area concentration can be obtained from the bubble interfacial velocity. In view of Eq. (10), Kataoka et al. [12,13] formulated a mathematical method to determine the local time-averaged interfacial area concentration for both double-sensor and four-sensor probes. In the application of the double-sensor probe, it was suggested that

$$\bar{a}^t_i(x_0, y_0, z_0) = 2N_t\overline{\frac{1}{|v_i|\cos\phi}} \tag{11}$$

with

$$\overline{\frac{1}{|v_i|}} = \frac{\sum_j \frac{1}{|v_{ij}|}}{\sum_j} \quad \text{and} \quad \overline{\frac{1}{\cos\phi}} = \frac{\sum_j \frac{1}{\cos\phi_j}}{\sum_j}, \tag{12}$$

where N_t is the number of bubbles which pass the point (x_0, y_0, z_0) per unit time, and ϕ_j is the angle between the unit normal of the jth interface and the

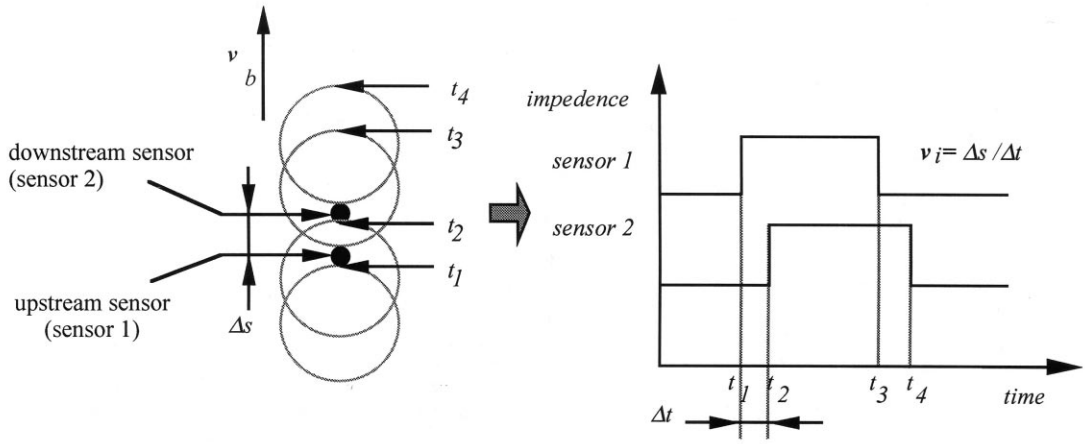

Fig. 1. Illustration of signals obtained by the sensor(s) of the conductivity probe.

interfacial velocity as shown in Fig. 2. In formulating Eq. (11), however, it was assumed that the bubbles were spherical, and every part of the bubble had equal probability of being intersected by the probe. It was also assumed that the angle between the bubble interfacial velocity and the axial direction, z, was random with an equal probability within some maximum angle, α_0.

The final expression for the local time-averaged interfacial area concentration by the double-sensor probe technique was then given by [13,14,16]

$$\bar{a}_{\mathrm{i}}^{\mathrm{t}}(x_0, y_0, z_0) = \frac{4N_{\mathrm{t}}\left\{\sum_j \frac{1}{|v_{szj}|} \Big/ \sum_j\right\}}{1 - \cot\frac{1}{2}\alpha_0 \ln\left(\cos\frac{1}{2}\alpha_0\right) - \tan\frac{1}{2}\alpha_0 \ln\left(\sin\frac{1}{2}\alpha_0\right)} \tag{13}$$

where α_0 was obtained by

$$\frac{\sin 2\alpha_0}{2\alpha_0} = \frac{1 - \left(\sigma_z^2/|\overline{v_{iz}}|^2\right)}{1 + 3\left(\sigma_z^2/|\overline{v_{iz}}|^2\right)} \tag{14}$$

Here v_{szj}, $|\overline{v_{ij}}|$ and σ_z are the z-component of the jth interfacial velocity, mean value of the z-component of the velocity, and the velocity fluctuations, respectively. Also, v_{szj} was defined by

$$|v_{szj}| \cos\mu_j = |v_{ij}| \cos\phi_j \tag{15}$$

where the angle μ_j was defined as the angle between the probe sensor and the normal surface vector as shown in Fig. 2. The reciprocal harmonic mean of $|v_{szj}|$ and the square mean of fluctuation σ_z^2 were further correlated with the probability density function. For detailed derivation, one should refer to the study done by Kataoka et al. [13,14].

In many two-phase flow systems, however, bubbles whose shapes vary significantly from spherical are frequently encountered and the application of the double-sensor probe becomes erroneous. This is where the application of a four-sensor conductivity probe becomes important. In the four-sensor conductivity probe, three pairs of double-sensor probes can be formed with one common sensor in the upstream and three independent sensors in the downstream. Therefore, three components of interfacial velocities can be obtained at a local point by measuring the time delay between the signals from three pairs of double-sensors. For example, when the directions of the three independent probes are chosen as the x, y, and z axes, the equation for the time-averaged a_{i} can be simplified as [13,14]

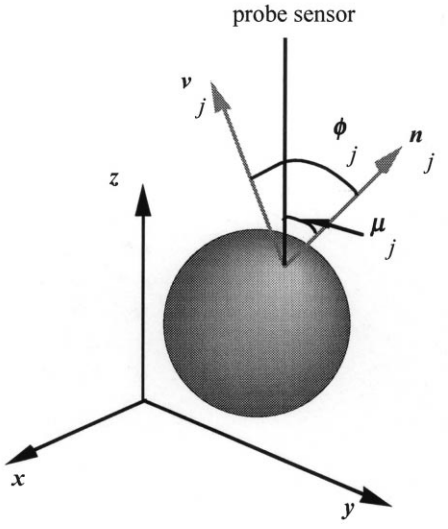

Fig. 2. Definition of angles ϕ_j and μ_j.

$$\bar{a}_{\mathrm{i}}^{\mathrm{t}} = \frac{1}{\Delta T}\sum_{j}\left[\left(\frac{1}{v_{\mathrm{s1}j}}\right)^2+\left(\frac{1}{v_{\mathrm{s2}j}}\right)^2+\left(\frac{1}{v_{\mathrm{s3}j}}\right)^2\right]^{1/2} \tag{16}$$

Therefore, unlike the double-sensor probe technique, no hypothesis for the bubble shape is necessary in the mathematical formulation to calculate the local interfacial area concentration. This allows the four-sensor probe to be applied in two-phase flow regimes where bubbles are no longer spherical in shape.

Some difficulties in applying the four-sensor conductivity probe, however, have been reported by previous studies [16,18]. The limitations were mainly caused by the size of the probe, such that the large measurement area or the spacing between the sensors caused a significant number of bubbles to miss some of the sensors. It was also reported that the deformation of the bubble interface could be significant as the bubble penetrates through the sensors. These shortcomings may lead to significant errors in estimating the local interfacial velocity. Due to such limitations, the four-sensor probe is yet to be applicable to general experiments. Moreover, application of the four-sensor probe is limited to larger bubbles, which prevents it from being employed in general two-phase flow conditions where various sizes of bubbles exist.

3. Development of the miniaturized conductivity probe and the signal processing scheme

To minimize the reported limitations discussed above, new designs are developed for the conductivity probe. These include both modified structures of the probe and new fabrication materials, which greatly enhance the capability of the probe. The new design and the selection of the fabrication material are based on known shortcomings, such as deformation of bubbles, oxidation of probe sensors, and missing bubble phenomenon.

3.1. Design of the miniaturized four-sensor probe

In fabricating the probe, gold acupuncture needles with its maximum OD of 0.13 mm are employed as sensors of the probe as shown in Fig. 3. High electrical conductivity of gold and sharply tapered tips, make the acupuncture needle ideal as sensors of the conductivity probe in reducing deformation of penetrating bubbles and minimizing the oxidation problem. For the dielectric coating of the probes, the conformal coating is used. Its low viscous (200 cps at 25°C), yet highly adhesive characteristics allow a very thin and uniform coating around the probe sensors with a coating thickness of less than 0.05 mm as can be seen in Fig. 3. It also has a high electrical resistivity of 4×10^4 Ω/cm, and strong water/chemical-proof characteristics, which are essential for two-phase experimental conditions. The final coating is completed using a commercial copper bond epoxy so as to form a firm bond between the junction of the probe sensors and the casing. After the final coating, the conductive ink is painted at the junctions to bond and to ensure electrical connections. A guage 11 (0.318 cm OD) stainless steel tube is used for the probe casing and it is reduced to a gauge 14 stainless steel tube to hold the sensor

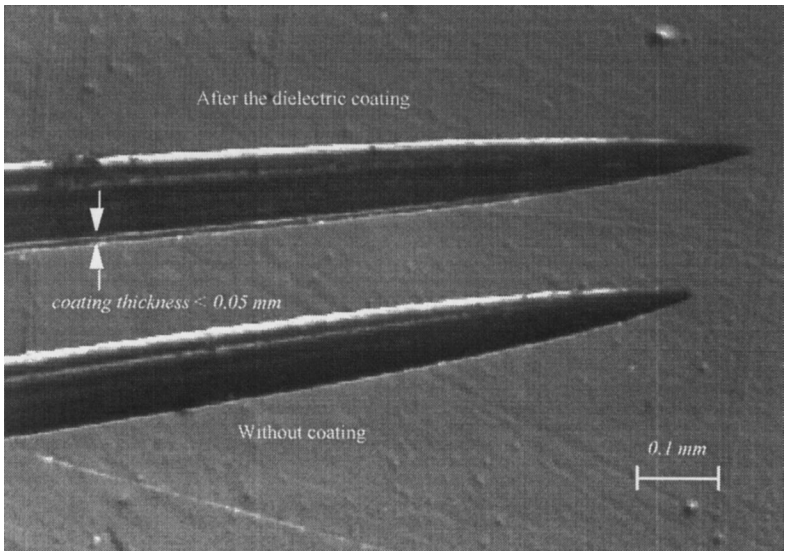

Fig. 3. Photographic image of the probe sensors with/without dielectric coating.

assembly. The casing is bent exactly at 90° without curvature.

Both the conventional and new designs of the probes are shown in Fig. 4. The significant reduction in the cross-sectional measurement area of the newly designed probe and the sharply tapered tips of the sensors can effectively minimize both the number of missing bubbles and the deformation of passing bubble interfaces. In fact, in the present experiments using the newly designed four-sensor conductivity probe, very few missing bubbles are found.

Another significant feature of the newly designed probe is that it accommodates a built-in double-sensor probe in the four-sensor configuration. Therefore, the newly designed four-sensor probe can be applied in a wide range of two-phase flow regimes spanning over bubbly, cap, slug, and churn-turbulent flows. This is a significant improvement in view of the interfacial area transport, because it allows one to observe how the local two-phase flow parameters develop along the flow field as the bubble size changes. The measurement area of the four-sensor probe used in the experiments is less than 0.2 mm^2 and the distance between the two tips of the double-sensor probe (sensors 0 and 1 in Fig. 4) is 2.4 mm. Here, the tip distance in the double-sensor part of the probe is based on the study by Wu and Ishii [21]. Hence, with the present probe configuration, the probe's range of measurable bubble diameter is form ~1 mm to Taylor bubbles.

In acquiring the signals from the sensors, a simple DC circuit is employed for simplicity of the device and for faster rise/fall time in the signals. It has been verified through experiments that the newly designed probe would last more than 1 year provided that the sensors are dried in the air after the experiments. The sampling frequency is varied between 6 and 10 kHz depending on the flow conditions, and an average of more than 2000 small bubble and 200 large bubble signals is acquired in slug flow conditions.

3.2. Signal processing scheme

The signal processing scheme developed for the newly designed conductivity probe is structured in two main parts; namely, the first part for conditioning acquired signals and the second part for processing the signals to obtain the desired two-phase flow parameters. The signal conditioning process includes filtration, normalization, and conversion of signals into step signals, whereas data processing consists of categorization, calculation, and correction processes. In processing the signals, the principles of obtaining interfacial area concentration with signals obtained from the double-sensor and four-sensor probes are different due to the fundamental difference in bubble shapes, measurement principles, and the geometry of the probes. In the following sections, the signal conditioning processes and the calculation principles of local time-averaged interfacial area concentration are discussed.

3.2.1. Signal conditioning

To obtain accurate local two-phase flow parameters, it is critical to identify the signals from the bubbles accurately. To accomplish this successfully, the signal processing scheme is constructed in several steps. They include moving median filtering process of the raw signals, normalization of the filtered signals, filtering

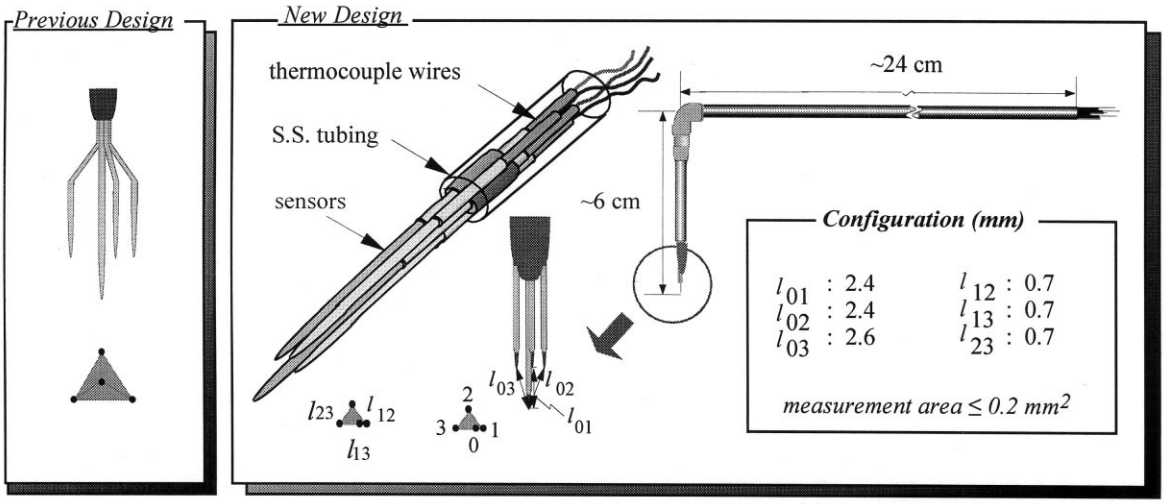

Fig. 4. Schematic diagrams of the conventional and new four-sensor conductivity probes.

noises through noise threshold, and generation of step signals.

It is likely that the signals obtained from the probe sensors contain some characteristic high frequency noises from other electronic devices. In such a case, the high frequency noises should be effectively removed to prevent significant error in estimating the interfacial area concentration. In order to filter these high frequency noises, the moving median filter scheme is employed. The algorithm of the moving median filter can be explained as follows: First, the initial data point of interest is selected. A consecutive odd number of data points (three or bigger) surrounding the point of interest are then selected as a group. In the given group of data points, the median value is found. This median value is then registered as the data point of interest in the filtered set of data. The next group is selected by advancing one data point from the previous data point of interest and grouping odd numbers of data points surrounding the new data of interest. This process is repeated until the final data point is reached. In the present experiments, the five-point moving median filter is employed. However, any odd number of data points equal or bigger than three can be chosen as a group for this filtering process.

Due to the finite rise/fall time of the signal and the different experimental conditions, neither the absolute value of the base voltage, nor the voltage drop is fixed. Therefore, all the signals obtained by the probe sensor should be normalized. This normalization can be calculated using

$$V_{\mathrm{norm},\,i} = \frac{V_{\mathrm{i}} - V_{\min}}{V_{\max} - V_{\min}} \tag{17}$$

where $V_{\mathrm{norm},\,i}$ is the normalized voltage of the ith signal, V_{i} is the ith signal, $V_{\max}$ is the maximum voltage, and $V_{\min}$ is the minimum voltage. Here, the minimum voltage is determined by the average voltage signal in the liquid phase. A simple way to determine the minimum voltage is to divide the total voltage range into four quarters, and set the most probable voltage in the lowest quarter as $V_{\min}$.

After the normalization, the remaining noises are removed by setting a threshold level. In principle, this level can be determined by finding the standard deviation of the fluctuations due to noise. In practice, however, the threshold level determined by an experimental observation can be acceptable if the fluctuations are not severe. In the present experiment, the threshold level of ± 0.05 V determined by experimental observation was an adequate level to remove noises. Therefore, any voltage fluctuations within ± 0.05 V are considered to be noise and are removed from the raw signals.

If the signals rise or fall instantaneously without any time delay when the bubbles pass through the probe sensors, the registering signals would be in step function form and the interfaces can be identified definitely. However, due to the finite rise/fall time in the signals, ambiguities in identifying the bubble interfaces can arise. Therefore, it is necessary that the raw signals obtained by the probe sensors be converted into step signals. In the present signal processing scheme, the criterion for converting the normalized signals into the square signals is constructed by determining the initiation of the bubble interface. When the acquired signal keeps rising (falling) more than five data points continuously above (below) the noise level, it is considered to be due to the bubble interface. After the bubble interface is detected, the signal is converted into a step function at the initial points. An example of signals converted from the normalized signals into the step signals is shown in Fig. 5.

3.2.2. Categorization of bubble signals

After the completion of the signal conditioning process, the signals are separated into spherical, distorted, cap, and Taylor bubbles depending on the bubble chord length information. This categorization process is possible due to the improved design of the new four-sensor probe, which accommodates both the double-sensor and four-senor probes. This categorization process is important in view of interfacial transport, because it allows one to study the transport phenomena of different types of bubbles independently.

In the present experiments, spherical and distorted bubbles are categorized as Group 1, and the cap and Taylor bubbles are categorized as Group 2. In identifying the bubble types, the maximum distorted bubble limit and the spherical bubble limit given by Ishii [24] and Ishii and Zuber [25] are used as criteria, such that

$$D_{\mathrm{ds}} = 4\sqrt{\frac{2\sigma}{g\Delta\rho}}N_{\mu_{\mathrm{f}}}^{1/3}; \quad \text{Spherical bubble limit} \tag{18}$$

and

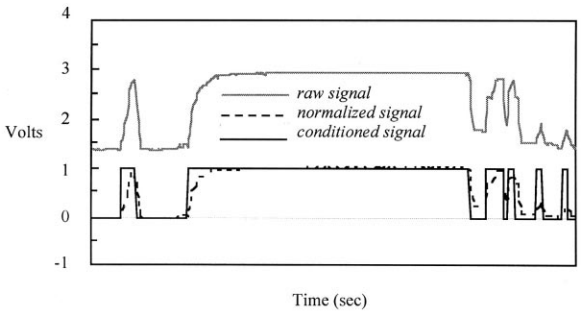

Fig. 5. The signals before and after the signal conditioning processes.

$$D_{\mathrm{dmax}} = 4\sqrt{\frac{\sigma}{g\Delta\rho}}; \quad \text{Maximum distorted bubble limit} \tag{19}$$

where

$$N_{\mu_{\mathrm{f}}} = \frac{\mu_{\mathrm{f}}}{\left(\rho_{\mathrm{f}}\sigma\sqrt{\frac{\sigma}{g\Delta\rho}}\right)^{1/2}} \tag{20}$$

Therefore, the bubbles whose chord lengths are smaller than D_{ds} are categorized as spherical bubbles, and those bigger than D_{ds} but smaller than D_{dmax} are categorized as distorted bubbles. In the present experiment, the Taylor bubble is defined as the bubble whose diameter is the same as the tube diameter. Hence, when the chord length of the bubble at the center of the tube is the same or bigger than the tube radius, it is categorized as a Taylor bubble. The cap bubbles are then categorized as those whose chord lengths are bigger than D_{dmax} and smaller than the Taylor bubble chord length.

In obtaining the void fraction and the bubble chord length, the common sensor (sensor 0 in Fig. 4) is used. For the interfacial area concentration, the signals from the double-sensor probe (sensors 0 and 1 in Fig. 4) are used for the spherical bubbles, whereas the signals from three pairs of double-sensor (sensors 0 and 1, 0 and 2, and 0 and 3 in Fig. 4) are used otherwise.

3.2.3. Calculation of the time-averaged interfacial area concentration

The measurement principle of the multi-sensor conductivity probe in obtaining local time-averaged interfacial area concentration, a_{i}, is based on the definition given by Ishii [1] as shown in Eq. (10). Based on this definition, Kataoka et al. [13,14] formulated a mathematical method to determine the local time-averaged a_{i} for both double-sensor probe and four-sensor probes by measuring the local interfacial velocity as shown in Eqs. (13) and (16), respectively. Since then, the equations have been improved [18,21–23] to account for the errors associated with measurement due to the limitations of the probe [16,18,21]. Such efforts have been made particularly on improving the double-sensor conductivity probe measurement. This is due to the fact that the measurement technique employing the double-sensor probe requires assumptions such as (a) the bubbles are spherical in shape (b) every part of the bubble has an equal probability of being intersected by the probe (c) the angle between the bubble interfacial velocity and the axial direction, z, is random with an equal probability within some maximum angle, α_0 and, (d) there is no fluctuation in the path of the penetrating bubble, and it passes through both sensors of the probe.

On the other hand, for the measurement employing the four-sensor probe, other phenomena should be carefully examined due to the characteristic shape of the large bubbles. When the bubble size is large compared to the separation distances of the sensors (l_{1i} where $i = 1, 2$ and 3 in Fig. 4) and when the bubble interface is not significantly distorted, the bubble penetrates all the four sensors. Such an event registers four consecutive signals from front and rear interfaces of passing bubbles, and the three components of the local interfacial velocity from front and rear interfaces can be calculated by the time delay information obtained from the signals. However, the interfaces of large bubbles are susceptible to significant distortions. Furthermore, in slug flow conditions, one of the probe sensors may miss the interface near the flow duct wall due to the characteristic liquid film formed near the wall.

In view of these, three kinds of bubble signals can be identified as signals that cannot be used in obtaining the local instantaneous interfacial velocity. The first kind occurs when a small spherical bubble misses one sensor of a double-sensor probe. In this case, only a single signal is registered, as illustrated in Fig. 6(a). The term '*missed*' or '*missing*' bubble signal refers to this case. The second kind is referred to as a '*non-effective*' bubble signal. When the interfaces of the bubbles are highly distorted, the signals due to the rear interfaces of the bubbles obtained by the common sensor may not precede the ones obtained by other rear sensors of the probe. When such signals are acquired, it is not possible to estimate the interfacial velocity, and those '*non-effective*' signals cannot be used in calculating the local a_{i}. An example of such signals is illustrated in Fig. 6(b). The third kind occurs due to the characteristic shape of Taylor bubbles. In slug flow conditions, a thin layer of liquid film exists between the Taylor bubble and the flow duct wall, by which a very steep interface is formed. When such a steep interface is encountered, the interface and the probe sensors become parallel to each other, and one of the probe sensors may miss the interface. An example of missing signals due to the steep Taylor bubble interface is shown in Fig. 6(c). This steep Taylor bubble interface is of great importance, because the major contribution in the interfacial area concentration of the Taylor bubbles is attributed to this interface. Therefore, proper estimation of such missing signals should be made. This missing phenomenon near the flow duct wall due to the steep interface of Taylor bubbles was also reported by Ishii and Revankar [16].

Recently, Wu and Ishii [21] suggested a correction method accounting for the missed interfaces of spherical bubbles in the application of the double-sensor conductivity probe. In this study, they considered the effects of the lateral movement of the bubbles and the probe tip spacing (l_{01} in Fig. 4). They divided the

measured bubbles in two categories, one for bubbles whose interface is moving normal to the probe and passing through both the sensors, and another for those missing one of the sensors of the probe. In their correction scheme, the mean value of the experimentally measured bubble interfacial velocity was rigorously related to the actual interfacial velocity of the bubbles by defining theoretical calibration factors. These calibration factors were employed to account for the bubbles whose interfaces move normal to the probe, and those missing one of the sensors. By determining the calibration factors, they modified the formula given by Kataoka et al. [13–15] as

$$\bar{a}_{\mathrm{i}}^{\mathrm{t}} = f_{\mathrm{total}}\left(\frac{2N_{\mathrm{b}}}{\Delta s \Delta T}\right)\left(\frac{\sum_{j}(\Delta t_j)}{N_{\mathrm{b}} - N_{\mathrm{miss}}}\right), \quad \text{for } \Delta s = 0.36D_{\mathrm{b}} \sim 0.86D_{\mathrm{b}} \tag{21}$$

with

$$f_{\mathrm{total}} = 2 + \left(\frac{v_{\mathrm{b}}'}{\overline{v_{\mathrm{b}}}}\right)^{2.25}, \quad \text{for } \Delta s = 0.36D_{\mathrm{b}} \sim 0.86D_{\mathrm{b}} \tag{22}$$

where N_{b} is the number of total bubbles obtained, v_{b}' is the fluctuation of bubble velocity, $\overline{v_{\mathrm{b}}}$ is the average bubble velocity obtained by effective signals, and Δt_j, ΔT, Δs are the time delay obtained by effective signals for the jth bubble interface, total sampling time at a local point, and distance between two tips of the sensors, respectively. Eq. (21) was found to be valid as long as the output signals from the probe were valid for bubble identification and the sample size was sufficiently large. For bubble sizes varying from 0.6 to 1.4 times the mean bubble size, it was found that the interfacial area concentration calculated by Eq. (21) would result in a statistical error of $\pm 7\%$ for a sample size of $\sim$1000 bubbles [21].

For bubbles whose shapes are not spherical, such as distorted, cap, or Taylor bubbles, the local time-averaged interfacial area concentration is obtained by the signals acquired from four sensors. Due to the irregular interfaces of larger bubbles, the contribution to a_{i} from the front and rear interfaces can be significantly different. Therefore, each interface should be considered separately. Hence, unlike the double-sensor method, each signal pair from the front and rear interface is considered independently in the calculation of interfacial area concentration. In the process of estimating the local interfacial velocity with the defective signals from distorted and cap bubbles, the corrections are made in two steps for both the non-effective signals and missing signals. First, when the non-effective rear signals are encountered, the corrections are made according to the average a_{i} acquired from effective rear signals as well as the total number of non-missing bubbles. Next, the missing bubble signals are corrected by the average contribution from both the effective and the total number of bubbles. This two-step correction method yields the equation for the total time-aver-

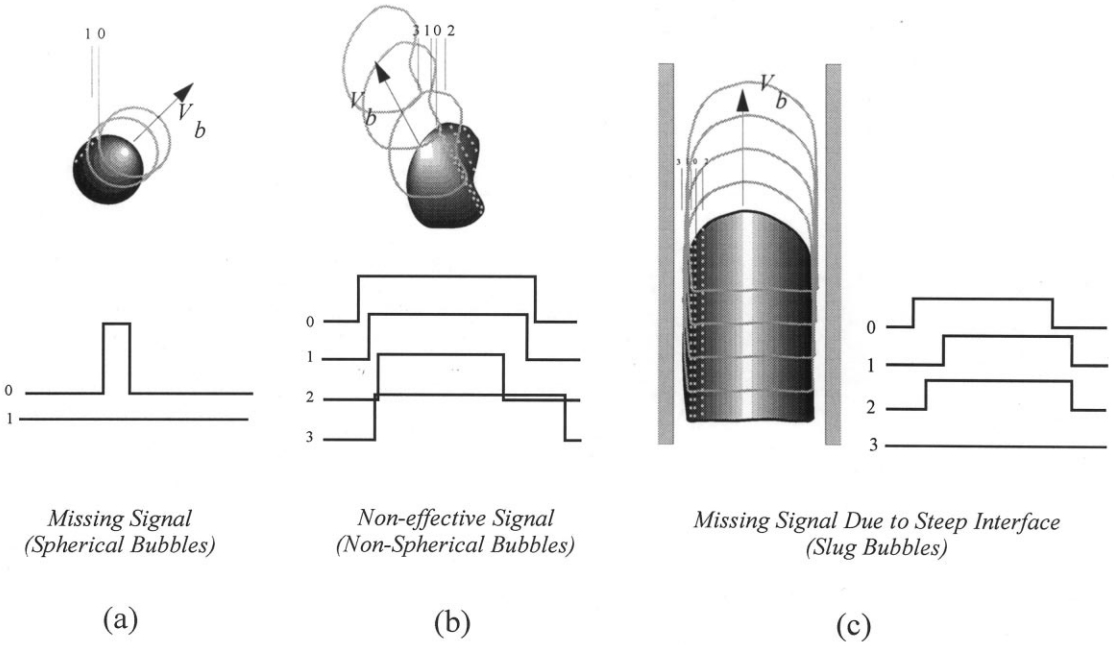

Fig. 6. Examples of defective signals.

aged a_i at a local point as

$$\bar{a}_{i,\,\mathrm{tot}} = \bar{a}_{if,\,\mathrm{eff}}\left(\frac{N_{\mathrm{tot}}}{N_{\mathrm{f,\,eff}}}\right) + \bar{a}_{ir,\,\mathrm{eff}}\left(\frac{N_{\mathrm{tot}}}{N_{\mathrm{r,\,eff}}}\right) \quad \text{for distorted and cap bubbles} \tag{23}$$

where $\bar{a}_{i,\,\mathrm{eff}}$ is the average a_i calculated with effective bubble signals, N_{eff} is the number of effective bubble signals, N_{tot} is the total number of bubbles counted by the common sensor, and f and r denote front and rear bubble interfaces, respectively.

In order to account for the missing signals due to the steep interface of Taylor bubbles near the flow duct wall, the correction method employed by Ishii and Revankar [16] can be applied. In their study, the interfacial area concentration was treated as the ratio of the surface area of the bubble interface to the volume formed by the measurement area of the four-sensor probe. The equation for the calculation of a_i of the missing Taylor bubble interfaces was then given by

$$\bar{a}_{i,\,\mathrm{miss}} = N_{\mathrm{miss}}\frac{t_b}{\Delta T}\frac{\bar{l}_s}{A_s} \tag{24}$$

where N_{miss} is the number of missing (steep) Taylor bubble interface, t_b is the residence time of the missing bubble signals, ΔT is the total sampling time, $\bar{l}_s$ is the average distance between three independent sensors (i.e., l_{12}, l_{13}, and l_{23} in Fig. 4), and A_s is the measurement area of the probe. Therefore, the total time-averaged a_i for the Taylor bubbles is obtained by

$$\bar{a}_{i,\,\mathrm{slug,\,tot}} = \bar{a}_{if,\,\mathrm{eff}}\left(\frac{N_{\mathrm{tot}}}{N_{\mathrm{f,\,eff}}}\right) + \bar{a}_{ir,\,\mathrm{eff}}\left(\frac{N_{\mathrm{tot}}}{N_{\mathrm{r,\,eff}}}\right) + \bar{a}_{i,\,\mathrm{miss}} \quad \text{for Taylor bubbles} \tag{25}$$

In Eq. (25), it should be noted that N_{tot} is the sum of the effective and non-effective interfaces *without* including the missing Taylor bubble interfaces.

In summary, the equations used in calculating the local time-averaged a_i in the present experimental study are: Eq. (21) is used in the calculation of the total a_i for the spherical bubbles using the signals obtained by the double-sensor probe. The equation given by Kataoka et al. [13,14,18] for the four-sensor conductivity probe is used in calculating a_i for distorted, cap, and Taylor bubbles with effective signals. Eqs. (23) and (25) are used in the calculation of the total a_i for distorted and cap bubbles, and the total a_i for the Taylor bubbles, respectively. The local time-averaged two-phase parameters obtained after the completion of the signal processing are (a) number of bubbles, (b) interfacial velocity, (c) void fraction, (d) interfacial area concentration, and (d) Sauter mean diameter of each type of bubble. The two-group parameters are obtained by summing the corresponding parameters, namely, Group 1 by summing the acquired parameters from the spherical and distorted bubbles, and Group 2 by summing those from the cap and Taylor bubbles.

4. Experiment

A schematic diagram of the vertical co-current two-phase flow experimental loop is shown in Fig. 7. The test section is made of a Lucite pipe of 5.08 cm ID with 375 cm in height. The de-mineralized water and air are supplied by a centrifugal pump and an air-compressor, respectively. Bubbles are generated through stainless steel hypodermic tubes of ID 0.12 mm, which are arranged in a 20×20 square matrix. After the two-phase mixing chamber, a Tee is employed to create larger bubbles. Bubbles escaping from the air chamber in the Tee assembly are then introduced into the test section through a horizontal tube followed by two 45° elbows. The liquid and gas flow rates are controlled by rotor meters. The probe is mounted on a support, which is designed such that the probe can be traversed by a micrometer. To capture images of bubbles, a SONY CCD VX-3, Hi-8 video camera is used at a frame rate of 30 frames/.

The gas flow rates are varied by $j_g = 0.052$, 0.179, and 0.432 m/s while the liquid flow rate is fixed at $j_f = 0.321$ m/s. The flow conditions are chosen such that the Taylor bubbles start to form at the lowest gas flow condition at $L/D = 32$. A simple DC circuit is employed to obtain the signals from the probe. The signal from the probe is imported to the personal computer by a data acquisition system. The imported signal is then processed by a personal computer. The sampling frequency is varied between 6 and 8 kHz depending on the flow conditions. More than 2000 bubbles of Group 1 and more than 200 bubbles of Group 2 are acquired at a local measurement point for the given sampling time. The probe is traversed at a fraction of 1.27 mm from the center to the wall of the test tube. The local time-averaged interfacial area concentration for spherical bubbles is acquired from the signals obtained by the built-in double-sensor unit, and that of other types of bubbles is acquired by the signals from four sensors of the probe.

The characteristic experimental results obtained by the four-sensor conductivity probe are shown in Fig. 8(a)–(c). The data shown in these figures are obtained at $L/D = 32$ with $j_g = 0.432$ m/s and $j_f = 0.321$ m/s. At this flow condition, the average chord length of the Taylor bubbles measured at the center of the flow duct by the common sensor is 17.2 cm. In

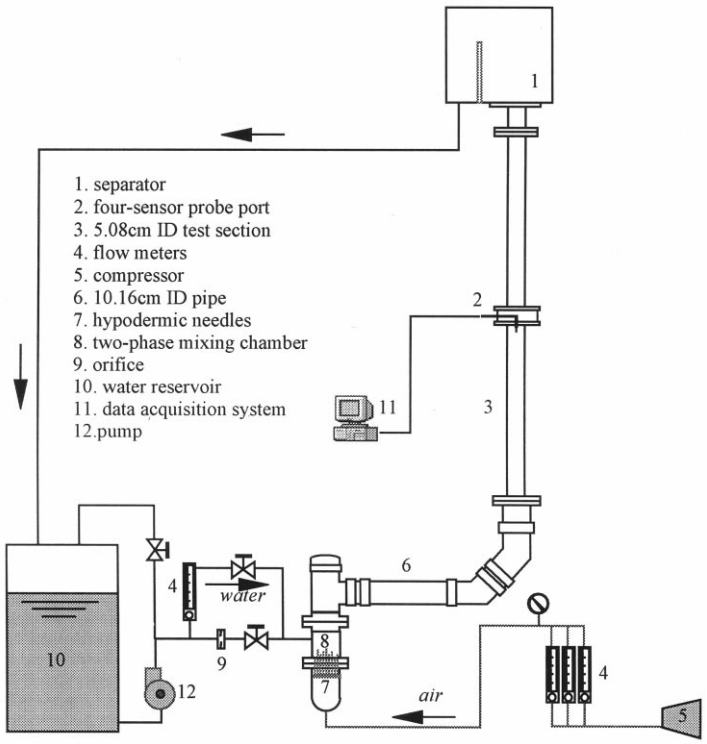

Fig. 7. Schematic diagram of the experimental loop designed for the benchmark experiment of the newly-designed miniaturized four-sensor conductivity probe.

Fig. 8(a), the profiles of the local time-averaged void fraction along the radial direction of the tube are plotted. Here, the void fractions are categorized into two groups, where Group 1 includes the spherical and distorted bubbles and Group 2 includes cap and Taylor bubbles. Also plotted in this figure is the total void fraction, which is the sum of the void fraction of two groups. The void fraction of the Group 2 bubbles peak at the center of the tube, while that of the Group 1 bubbles remains nearly uniform across the flow duct. Under this flow condition, the contribution to the void fraction from Group 1 bubbles is about 20% of the

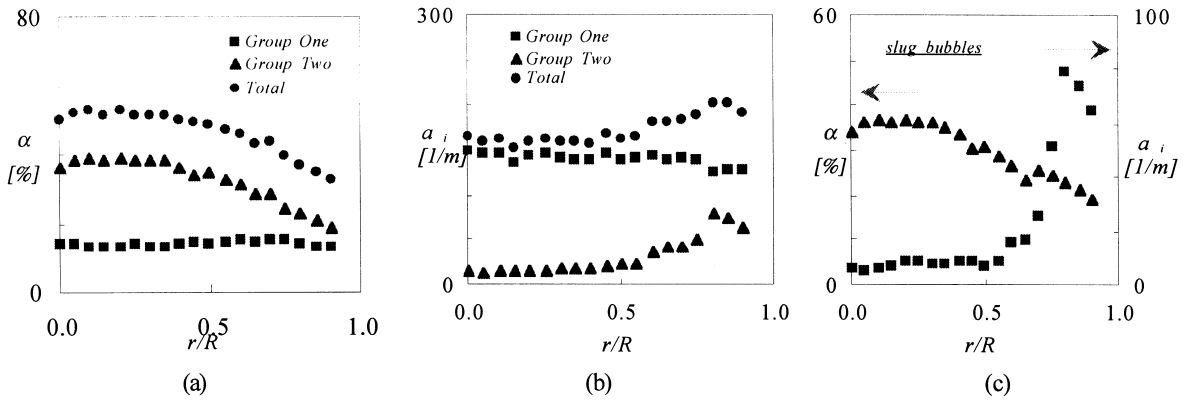

Fig. 8. The characteristic experimental results obtained by the four-sensor conductivity probe at $L/D = 32$ with $j_g = 0.432$ m/s and $j_f = 0.321$ m/s. The time-averaged local (a) void fraction and (b) interfacial area concentration of Group 1 and Group 2 bubbles, and (c) for Taylor bubbles.

total void fraction, and the total void fraction is determined mainly by the Group 2 bubbles. The profiles of the local time-averaged interfacial area concentration are shown in Fig. 8(b). In the interfacial area concentration profiles of the Group 2 bubbles, a local peak near the pipe wall is observed. Unlike the void fraction, the major contribution to total interfacial area concentration is due to the Group 1 bubbles. To highlight the contribution of the Taylor bubbles, the local time-averaged void fraction and the interfacial area concentration of the Taylor bubbles are plotted in Fig. 8(c). The center peak in the void profile and the sharp wall peak in the interfacial area concentration profile clearly demonstrate the characteristic signature of the Taylor bubbles. Comparing Fig. 8(c) with (b), it can be seen that the void fraction of the Group 2 bubbles is determined mainly by the Taylor bubble.

In Fig. 9(a)–(d), the local two-phase parameters at $L/D = 32$ in three different flow conditions are compared for Group 1 and Group 2 bubbles. As shown in the figures, both void fraction and interfacial area concentration increase with increasing gas flow rates for Group 1 and Group 2 bubbles. The increase in the void fraction and the local wall peak in the interfacial area concentration profile of Group 2 bubbles indicate that the length of the Taylor bubble becomes longer, and the contribution from the side interface of the Taylor bubbles in local a_i becomes more significant with increasing gas flow rates. Moreover, the local a_i of the Group 2 bubbles remains unchanged between the tube center and $r/R \cong 0.5$. This implies that the shapes of the nose of Taylor bubbles do not change significantly regardless of the bubble chord length.

In view of axial development of the two-phase parameters, the local void fraction and the interfacial area concentration measured at $L/D = 32$ and 64 are plotted in Figs. 10 and 12, respectively. In Fig. 10(a)–(c), the local time-averaged void fraction of Group 1 and Group 2 bubbles measured at $L/D = 32$ and 64 are compared for three different flow conditions. In Fig. 10(d), profiles of the time-averaged local Sauter mean diameter of Group 1 bubbles for all cases are plotted. Here, the Sauter mean diameter is calculated by

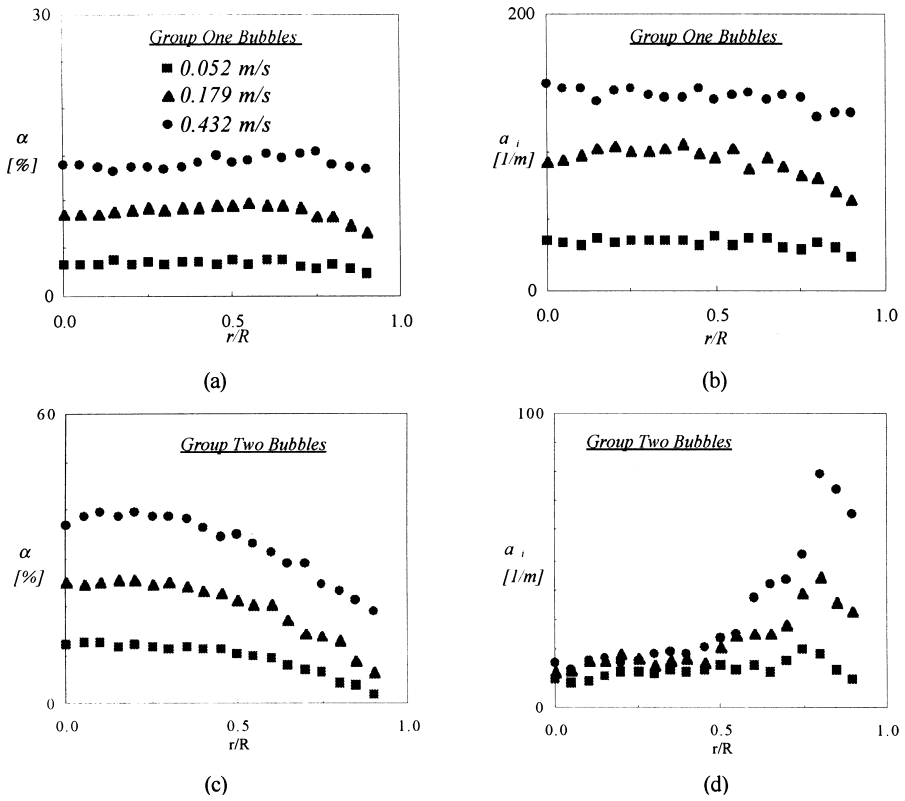

Fig. 9. Local time-averaged void fraction and interfacial area concentration in three different flow conditions for (a) and (b) for Group 1 and (c) and (d) Group 2 bubbles; $j_f = 0.321$ m/s and j_g varied.

$$D_{\text{sim}} = \frac{6\alpha}{a_{\text{i}}}. \tag{26}$$

As shown in Fig. 10(a)–(c), the void fraction of Group 1 bubbles increases along the axial direction for all flow conditions. The Sauter mean diameters of Group 1 bubbles, however, remain nearly uniform regardless of both flow conditions or axial locations. This implies that both the interfacial area concentration and void fraction of the Group 1 bubbles increase. Hence, the number of Group 1 bubbles increases with increasing gas flow rates and along the downstream of the flow duct.

In Fig. 11, the void fraction and interfacial area concentration for the Taylor bubbles are plotted for two different axial locations. As shown in Fig. 11(a), the void fraction of Taylor bubbles increases with increasing axial location, whereas in Fig. 11(b) and (c) it remains nearly the same. This is due to the coalescence of Taylor bubbles in the downstream, which results in a decrease in the number of Taylor bubbles and increase in the Taylor bubble length. Also, the local peak in the a_{i} near the wall increases along the axial direction in all flow conditions, which reflects longer side interfaces of Taylor bubbles. The a_{i} near the center of the tube, however, remains quite uniform for all the flow conditions suggesting that the contour of the slug nose doesn't depend significantly on the length of the Taylor bubble.

5. Benchmark of the new four-sensor conductivity probe technique

In order to benchmark the newly developed conductivity probe and its signal processing scheme, an image analysis method is employed. In benchmarking the double sensor conductivity probe, the images captured in a bubbly flow are analyzed, whereas the Taylor bubble images are used in benchmarking the four-sensor conductivity probe.

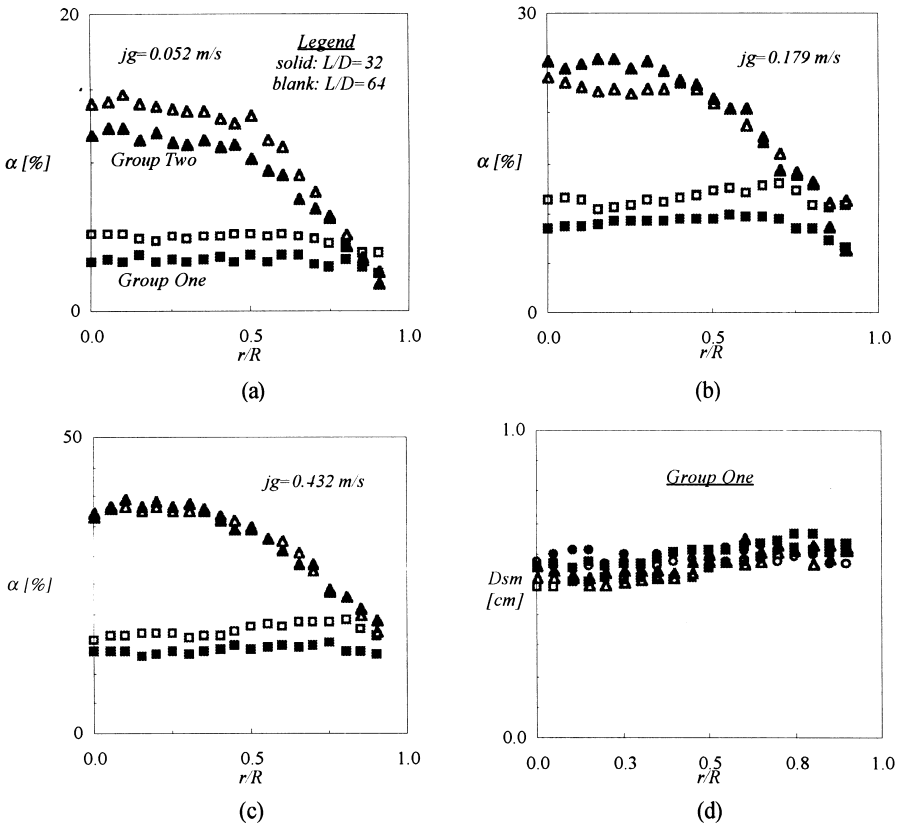

Fig. 10. Development of void fraction and Sauter mean diameter along the axial direction of the flow duct. Solid data points measured at $L/D = 32$ and Blank data points measured at $L/D = 64$. $j_{\text{f}} = 0.321$ m/s and (a) $j_{\text{g}} = 0.052$ m/s, (b) $j_{\text{g}} = 0.179$ m/s, (c) $j_{\text{g}} = 0.432$ m/s, and (d) Sauter mean diameters of Group 1 bubbles.

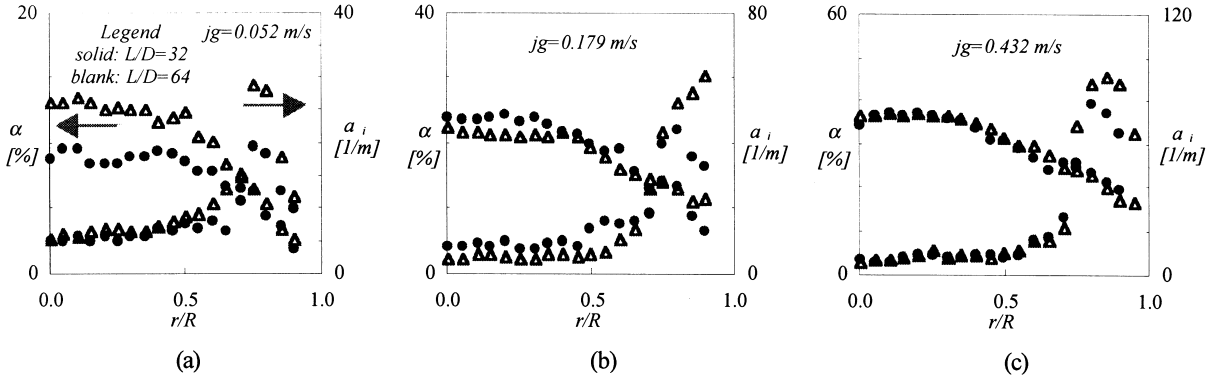

Fig. 11. Development of two-phase parameters for Taylor bubbles in three different flow conditions. Solid data points at $L/D = 32$ and blank data points at $L/D = 64$.

5.1. Benchmark of the double-sensor conductivity probe

The benchmark experiments for the double-sensor probe are performed in an acrylic vertical rectangular flow duct in air–water two-phase mixture [26]. The rectangular flow duct is ideal in view of reducing image distortion. A rectangular window of 100 × 62 mm in size is prepared at the same location where the measurements are made by the double-sensor conductivity probe. The images of the bubbly flow are captured by a SONY CCD VX-3, Hi-8 video camera at a frame rate of 30 frames/sec. The void fraction of the two-phase mixture is controlled, so that it is below 5% in order to prevent the bubble images from overlapping. A computer code developed by Zhang and Ishii [27] is used to process the captured images to obtain the location and the diameter of each bubble in a given frame. An example of the photographic images used in image analysis and the coordinate system employed in the image analysis is shown in Fig. 12. Here the image is captured at the flow condition of $j_g = 0.023$ m/s and $j_f = 0.315$ m/s. The y–z plane, or (flow duct depth) × (window height), area-averaged interfacial area concentration at any position x is then calculated by

$$\langle a_i(x)\rangle_{yz} = \frac{\pi \sum_j (D_b(x))_j}{A_{yz}} \tag{27}$$

where $D_b(x)$ is the bubble diameter at location x, and A_{yz} is the product of image height and flow duct depth. In order to effectively compare the data obtained by the double-sensor conductivity probe, the

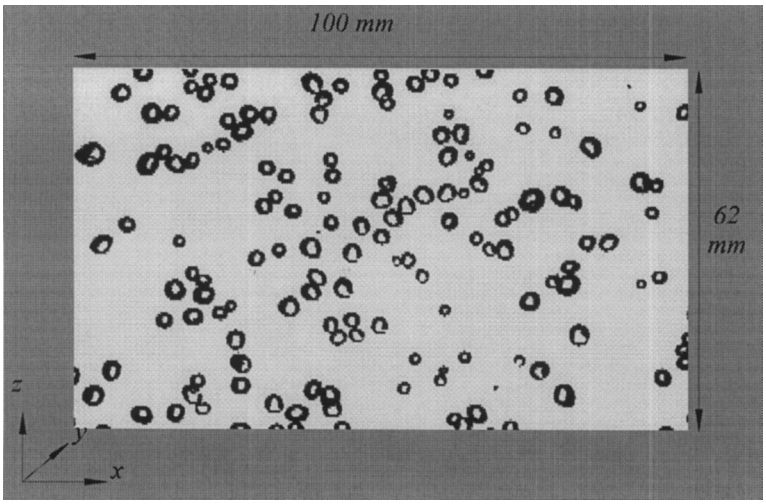

Fig. 12. Photographic image captured for image analysis in benchmarking the double-sensor conductivity probe and its coordinate system. $j_g = 0.023$ m/s and $j_f = 0.315$ m/s.

local time-averaged interfacial area concentration acquired along the x-direction should be line-averaged along the y-direction. Therefore, in obtaining the experimental values, the probe is traversed in half-width of the flow duct gap from the center to the wall by a fraction of 1 mm assuming that the flow is symmetric along the y-direction. The equivalent values of the interfacial area concentration measured by the probe to the values from image analysis method is then given by

$$\langle a_i(x)\rangle_{y,\,\text{probe}} = \frac{1}{L_y}\int_0^{L_y} \bar{a}_i^t \, dy, \tag{28}$$

where L_y is the total length of the flow duct gap width.

The typical result from a number of experiments is shown in Fig. 13. The relative percent difference between the two methods is within $\pm 10\%$. Considering the limitation of the image method near the edge of the viewing window (as shown in Fig. 12), the agreement is acceptable.

5.2. Benchmark of the four-sensor conductivity probe

The four-sensor conductivity probe is benchmarked by a number of images of Taylor bubbles with different lengths captured by video camera. The stable Taylor bubbles are generated in the stagnant liquid test column. Three typical images of Taylor bubbles of different lengths are shown in Fig. 14. From the captured images, the contour of the Taylor bubble is calculated with respect to the slug length assuming symmetric front and flat rear interfaces. According to

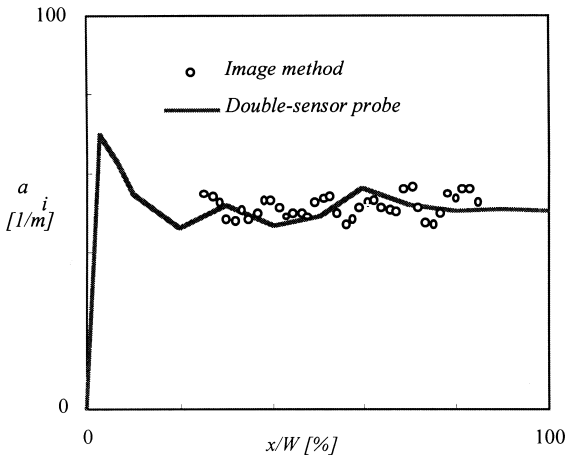

Fig. 13. Typical results obtained from the comparison between the interfacial area concentration measured by the double-sensor probe and that from image analysis. Here, W = half-width of the total flow duct width in the x-direction.

the images analyzed, the 6th order polynomial is found to best fit all of the interfacial profiles of the captured images.

When the contour function $f(r)$ is determined, the local void fraction and the interfacial area concentration are calculated by [16]

$$\alpha(r) = \left(1 - \frac{f(r)}{L_s}\right) N_s \frac{L_s}{v_s}, \tag{29}$$

and

$$a_i(r) = \left(1 + \sqrt{\left(\frac{df}{dr}\right)^2 + 1}\right) \frac{N_s}{v_s}, \tag{30}$$

where L_s is the Taylor bubble chord length, N_s is the number of Taylor bubbles counted by the probe per second, and v_s is the Taylor bubble rise velocity.

The comparisons between the values calculated based on the image analysis and the ones obtained by the four-sensor probe are shown in Fig. 15. In the figures, the solid line represents the calculated value, and the squares represent the data acquired by the probe. The agreement between the calculated values and the experimental data is quite acceptable in both void fraction and interfacial area concentration comparisons. Here, some deviations between the calculated values and the experimental data can be mainly attributed to the error in estimating the Taylor bubble chord-length. Since there can be variations in the Taylor bubble length at given flow conditions, the calculated values based on the average Taylor bubble length can cause a significant error. Another reason for deviation can be found from the fact that the image analysis is based on the smooth front and flat rear interfaces of stable Taylor bubbles, while the actual contour of the Taylor bubbles can be highly distorted. Also noted is that the Taylor bubble is assumed to be symmetric when the contour of the Taylor bubble is calculated, whereas the actual Taylor bubble nose deviates from the center.

To further check the reliability of the four-sensor conductivity probe measurement, the measured and calculated void fraction and interfacial area concentration are area-averaged and compared with each other. The results are shown in Fig. 16(a) and (b). In most cases, the agreement is good within $\pm 10\%$ difference. Thus, accounting for the average effect of the image calculation and the effect of distorted interfaces of the actual Taylor bubbles, it can be concluded that the agreement between the calculated values and the experimental data is good.

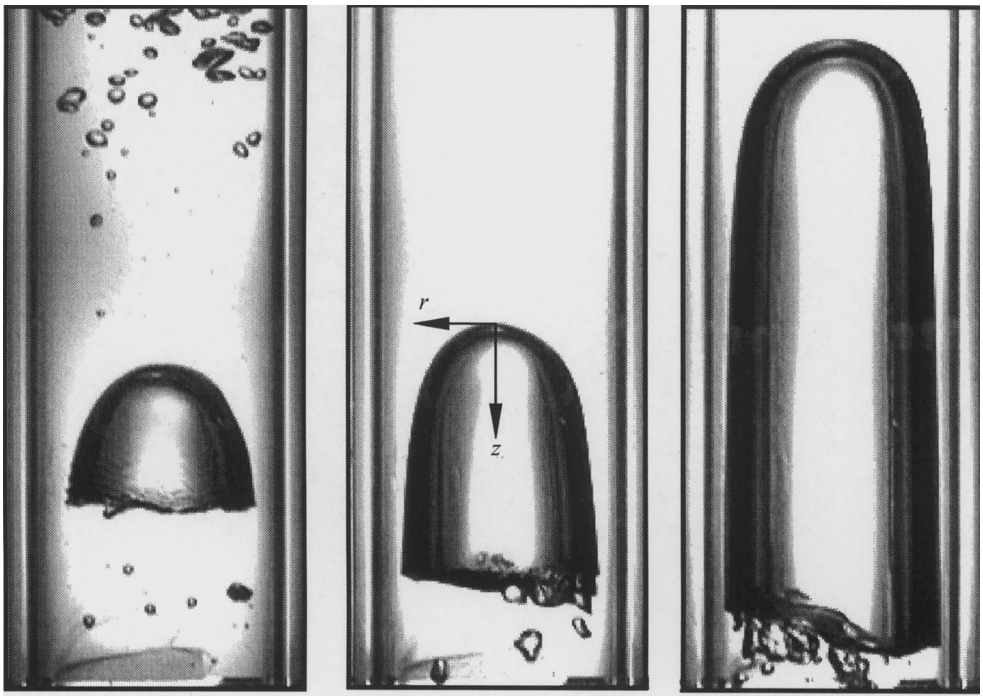

Fig. 14. Examples of Taylor bubble images captured by CCD camera. The frame size shown here; width = 6.35 cm and length = 14.55 cm.

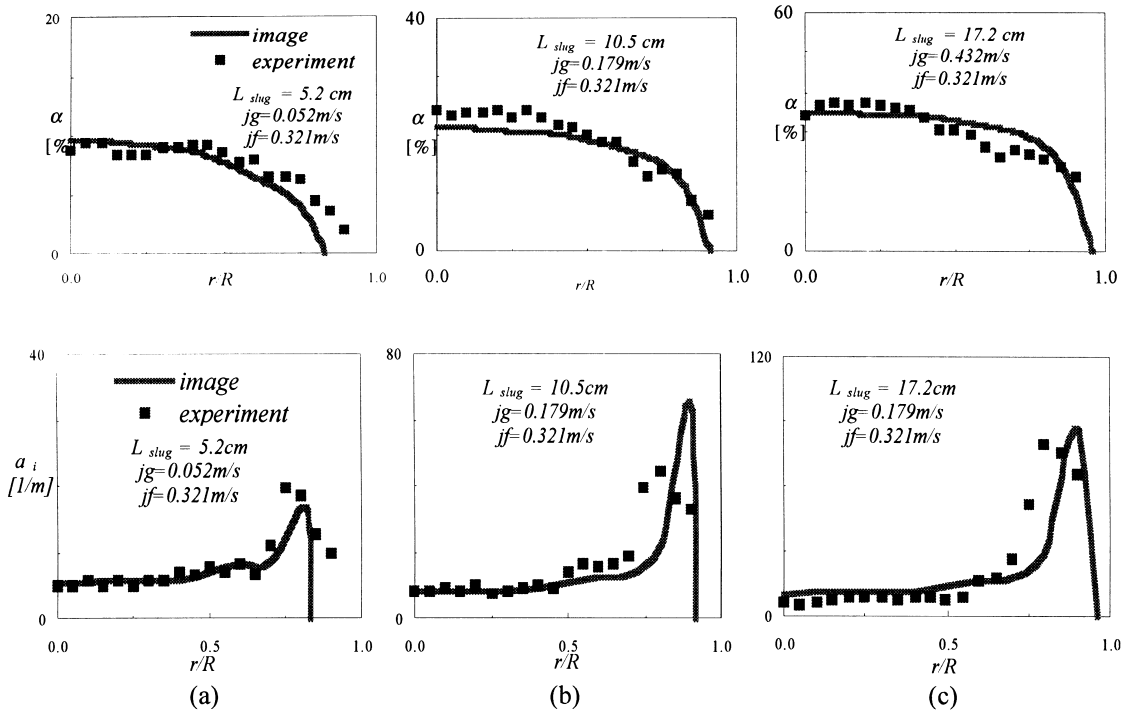

Fig. 15. Comparison of the void fraction and interfacial area concentration between the experimental data and the values calculated based on the image analysis for flow conditions; j_f fixed at 0.321 m/s and j_g varied at (a) $j_g = 0.052$ m/s, (b) $j_g = 0.179$ m/s, and (c) $j_g = 0.432$ m/s.

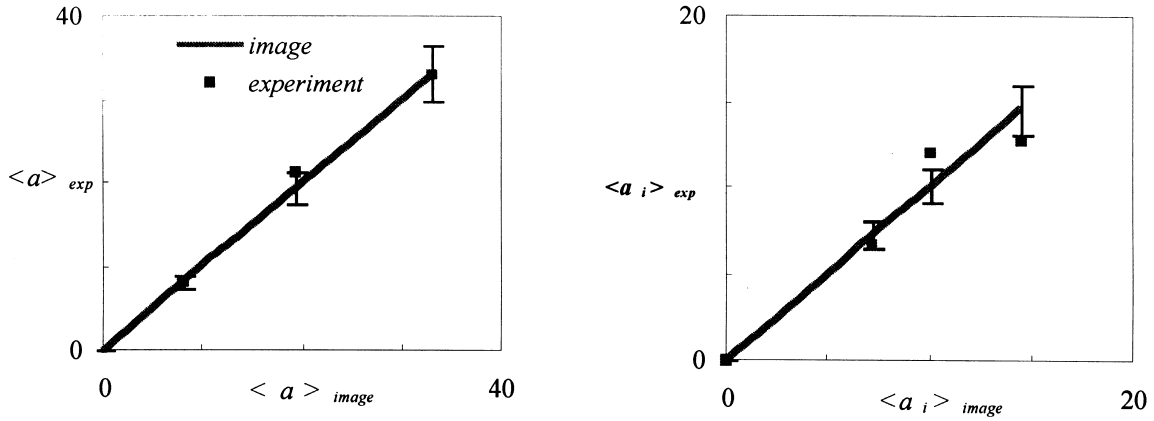

Fig. 16. Comparison between the area-averaged values of measured and calculated void fraction and interfacial area. Error bars shown here ±10%.

6. Summary and conclusions

The measurement of the local interfacial area concentration in two-phase flows is of great importance not only in assessing the capability of the heat or mass transfer of the given system, but also in establishing the closure relation in the two-fluid model. In view of this, a miniaturized four-sensor conductivity probe and its signal processing scheme are developed in this study. The sharp and highly conductive sensor tips, and miniaturized structure of the probe configuration can effectively minimize bubble deformation and missing bubble phenomena. Moreover, the new design accommodates the capability of a double-sensor probe for small bubbles, such that the two-phase parameters for both small and large bubbles can be obtained simultaneously. This is a significant improvement in view of building a database for the development of the two-group interfacial transport equation, because the new probe can be applied in flow conditions where different types of bubbles exist simultaneously. The signal processing scheme is constructed such that the two-phase flow parameters of the different types of bubbles can be separated and categorized accordingly. In the present study, the bubbles are categorized into two groups, such that Group 1 includes spherical and distorted bubbles and Group 2 includes cap and Taylor bubbles. Correction methods for missing and non-effective bubbles signals in calculating the local interfacial area concentration are formulated accounting for different contributions from various bubble interfaces.

The experimental data are obtained by the four-sensor conductivity probe at two different axial locations in three flow conditions. The results show characteristic signatures of both small and large bubbles. The time-averaged local void fraction and interfacial area concentration increase with increasing gas flow rates. The increase in Taylor bubble length and its steep side interface is well represented by the increase in the local wall-peak in the a_i profiles of Taylor bubbles. The development of local two-phase flow parameters along the axial direction of the flow duct is observed. The Sauter mean diameter of the Group 1 bubbles remains nearly uniform regardless of either flow conditions or the axial locations. This implies that the number of Group 1 bubbles increases with increasing gas flow rates and downstream of the flow. The number of Taylor bubbles, however, reduces as the length of the Taylor bubble increases, as reflected in the void fraction profiles.

Measurements made from both the double-sensor probe and the four-sensor probe are benchmarked by the theoretical calculations based on image analysis. Small deviations between the calculated and experimental values are observed. Nevertheless, accounting for the limiations of the image analysis, the agreement between the theoretical calculations and the experimental data is acceptable. With the newly designed four-sensor conductivity probe, the characteristic signatures of the various types of bubbles are well represented and quantified, which assess both the measurement principle and the capability of the probe.

Acknowledgements

The authors wish to express their sincere appreciation to Drs. R. Goulard and R. Price of DOE/BES for their support. This study was performed at Purdue University under the auspices of the U.S. Department of Energy.

References

[1] M. Ishii, Thermo-fluid dynamic theory of two-phase flow, in: Collection de la Direction des Etudes et Recherches d'Electricite de France, Eyrolles, Paris, 1975.

[2] M. Ishii, K. Mishima, Study of two-fluid model and interfacial area, Argonne National Laboratory Report, ANL-80-111, 1980.

[3] M. Ishii, K. Mishima, Two-fluid model and hydrodynamic constitutive relations, Nuclear Eng. and Design 82 (1984) 107–126.

[4] T.C. Chawla, M. Ishii, Two-fluid model of two-phase flow in a pin bundle of a nuclear reactor, Int. J. Heat and Mass Transfer 23 (1980) 991.

[5] M. Ishii, N. Zuber, Drag coefficient and relative velocity in bubbly, droplet or particulate flows, AIChE J. 25 (1979) p843.

[6] M. Ishii, K. Mishima, Study of two-fluid model and interfacial area, Argonne National Laboratory Report, ANL-80-111, 1980.

[7] M. Ishii, K. Mishima, Two-fluid model and hydrodynamic constitutive relations, Nuclear Eng. and Design 82 (1984) 107–126.

[8] N. Zuber, On the dispersed two-phase flow on the laminar flow regime, Chem. Eng. Sci. 19 (1964) 897.

[9] G. Kocamustafaogullari, M. Ishii, Foundation of the interfacial area transport equation and its closure relations, Int. J. Heat Mass Transfer 38 (3) (1995) 481–493.

[10] J.N. Reyes, Statistically derived conservation equations for fluid particle flows, in: Proceedings of ANS-THD, Vol. 5, ANS Winter Meeting, San Francisco, 1989, pp. 12–19.

[11] Q. Wu, S. Kim, M. Ishii, S.G. Beus, One-group interfacial area transport in vertical bubbly flow, Int. J. Heat Mass Transfer 41 (8/9) (1998) 1103–1112.

[12] L.G. Neal, S.G. Bankoff, A high resolution resistivity probe for determination of local void properties in gas–liquid flow, AIChE J. 9 (1963) 490–494.

[13] I. Kataoka, M. Ishii, A. Serizawa, Local formulation of interfacial area and its measurements in two-phase flow, Argonne National Laboratory Report, ANL-84-68, NUREG/CR-4029, 1984.

[14] I. Kataoka, M. Ishii, A. Serizawa, Local formulation and measurements of interfacial area concentration in two-phase flow, Int. J. Multiphase Flow 12 (4) (1986) 505–529.

[15] I. Kataoka, A. Serizawa, Interfacial area concentration in bubbly flow, Nuclear Eng. Design 120 (1990) 163–180.

[16] M. Ishii, S.T. Revankar, Measurement of interfacial area using four-sensor probe in two-phase flow, Purdue University Report, PU NE-91-1, 1991.

[17] S.T. Revankar, M. Ishii, Local interfacial area measurement in bubbly flow, Int. J. Heat Mass Transfer 35 (4) (1992) 913–925.

[18] I. Kataoka, M. Ishii, A. Serizawa, Sensitivity analysis of bubble size and probe geometry on the measurements of interfacial area concentration in gas–liquid two-phase flow, Nuclear Eng. Design 146 (1994) 53–70.

[19] G. Kocamustafaogullari, W.D. Huang, J. Razi, Measurement and modeling of averaged void fraction, bubble size and interfacial area, Nuclear Eng. and Design 148 (1994) 437–453.

[20] W.H. Leung, S.T. Revenkar, Y. Ishii, M. Ishii, Axial development of interfacial area and void concentration profiles measured by double-sensor probe method, Int. J. Multiphase Flow 38 (3) (1995) 445–453.

[21] Q. Wu, M. Ishii, Sensitivity study on double-sensor conductivity probe for the measurement of interfacial area concentration in bubbly flow, Int. J. Multiphase Flow 25 (1) (1999) 155–173.

[22] S. Kim, X.Y. Fu, X. Wang, M. Ishii, The local interfacial area concentration measurement in a two-phase flow using a four-sensor conductivity probe, in: ANS Transactions, 1998 ANS Winter Meeting, Washington DC, Nov. 15–19, TANSAO Vol. 79, 1998, p. 356.

[23] M. Ishii, Y. Mi, L.H. Tsoukalas, S. Kim, New objective approaches for characterization of interfacial structures in two-phase flow, in: Keynote Lecture, 1998 IMECE, Anaheim, CA, Nov. 15–20, 1998.

[24] M. Ishii, One-dimensional drift-flux model and constitutive equations for relative motion between phases in various two-phase flow regimes, Argonne National Laboratory Report, ANS-77-47, 1977.

[25] M. Ishii, Z. Zuber, Drag coefficient and relative velocity in bubbly, droplet or particulate flows, AIChE J. 25 (1979) 843.

[26] Q. Wu, S. Kim, D. McCreary, M. Ishii, S.G. Beus, Measurement of interfacial area concentration in two-phase bubbly flow, in: ANS Transactions, 1997 ANS Winter Meeting, Albuquerque, NM, Nov. 10–20, TANSAO 77, 1997, p. 437.

[27] G. Zhang, M. Ishii, Isokinetic sampling probe and image processing system for droplet size measurement in two-phase flow, Int. J. Heat and Mass Transfer 38 (1995) 2019.